

FIG. 4 a, Conversion of [1-¹³C] propionyl CoA to triketide lactone by DEBS 1+TE; b, conversion of [2,3-¹³C₂]-**3** to triketide lactone by DEBS 1+TE.

new polyketide structures through the engineering of combinations of PKS modules. Given the structural complexity of most natural or engineered products of modular PKSs 'one-pot' enzymatic synthetic methodologies could be an attractive complement to established chemical synthesis efforts aimed at elucidating the structure-activity relationships of lead molecules with potential human therapeutic, veterinary or agrochemical utility.

Note added in proof: Detection of cell-free activity of DEBS 1+TE has recently been reported elsewhere³⁵. □

Received 25 July; accepted 3 October 1995.

1. Cortes, J., Haydock, S. F., Roberts, G. A., Beville, D. J. & Leadlay, P. F. *Nature* **348**, 176–178 (1990).

2. Donadio, S., Staver, M. J., McAlpine, J. B., Swanson, S. J. & Katz, L. *Science* **252**, 675–679 (1991).
3. MacNeil, D. J. *et al. Gene* **115**, 119–125 (1992).
4. Schwecke, T. *et al. Proc. natn. Acad. Sci. U.S.A.* **92**, 7839–7843 (1995).
5. Cane, D. E. & Yang, C. C. *J. Am. chem. Soc.* **109**, 1255–1257 (1987).
6. Yue, S., Duncan, J. S., Yamamoto, Y. & Hutchinson, C. R. *J. Am. chem. Soc.* **109**, 1253–1255 (1987).
7. Cane, D. E., Prabhakaran, P. C., Tan, W. & Ott, W. R. *Tetrahedron Lett.* **32**, 5457–5460 (1991).
8. Cane, D. E., Lambalot, R. H., Prabhakaran, P. C. & Ott, W. R. *J. Am. chem. Soc.* **115**, 522–566 (1993).
9. Dutton, C. J., Hooper, A. M., Leadlay, P. F. & Staunton, J. *Tetrahedron Lett.* **35**, 327–330 (1994).
10. Cane, D. E. & Luo, G. *J. Am. chem. Soc.* **117**, 6633–6634 (1995).
11. Donadio, S., McAlpine, J. B., Sheldon, P. J., Jackson, M. & Katz, L. *Proc. natn. Acad. Sci. U.S.A.* **90**, 7119–7123 (1993).
12. Kao, C. M., Luo, G., Katz, L., Cane, D. E. & Khosla, C. *J. Am. chem. Soc.* **116**, 11612–11613 (1994).
13. Kao, C. M., Luo, G., Katz, L., Cane, D. E. & Khosla, C. *J. Am. chem. Soc.* **117**, 9105–9106 (1995).
14. Cortes, J. *et al. Science* **268**, 1487–1489 (1995).
15. Brown, M. J. B., Cortes, J., Cutter, A. L., Leadlay, P. F. & Staunton, J. *J. chem. Soc. chem. Commun.* 1517–1518 (1995).
16. Wakil, S. J. *Biochemistry* **28**, 4523–4530 (1989).
17. O'Hagan, D. *The Polyketide Metabolites* (Norwood, Chichester, 1991).
18. Katz, L. & Donadio, S. A. *Rev. Microbiol.* **47**, 875–912 (1993).
19. Kao, C. M., Katz, L. & Khosla, C. *Science* **265**, 509–512 (1994).
20. Marsden, A. F. A. *et al. Science* **263**, 378–380 (1994).
21. Wawszkiewicz, E. J. & Lynen, F. *Biochem. Zbl.* **340**, 213–227 (1964).
22. Corcoran, J. W. in *Antibiotics IV. Biosynthesis* (ed. Corcoran, J. W.) 146–148 (Springer, New York, 1981).
23. Roberts, G. & Leadlay, P. F. *Biochem. Soc. Trans.* **12**, 642–643 (1984).
24. Hunaiti, A. A. & Kolattukudy, P. E. *Antimicrob. Agents Chemother.* **25**, 173–178 (1984).
25. Caffrey, P., Beville, D. J., Staunton, J. & Leadlay, P. F. *FEBS Lett.* **304**, 225–228 (1992).
26. Leadlay, P. F. *et al. Biochem. Soc. Trans.* **21**, 218–222 (1993).
27. Dimroth, P., Walter, H. & Lynen, F. *Eur. J. Biochem.* **13**, 98–110 (1970).
28. Lanz, T., Tropf, S., Marner, F. J., Schröder, J. & Schröder, G. *J. biol. Chem.* **266**, 9971–9976 (1991).
29. Shen, B. & Hutchinson, C. R. *Science* **262**, 1535–1540 (1993).
30. Offenzeller, M. *et al. J. biol. Chem.* **268**, 26127–26134 (1993).
31. Cane, D. E., Luo, G., Khosla, C., Kao, C. M. & Katz, L. *J. Antibiot.* **48**, 647–651 (1995).
32. Plate, C. A., Joshi, V. C. & Wakil, S. J. *J. biol. Chem.* **245**, 2868–2875 (1970).
33. D'Agnoio, G. *et al. Biochim. biophys. Acta* **326**, 155–166 (1973).
34. Pieper, R., Luo, G., Cane, D. E. & Khosla, C. *J. Am. chem. Soc.* (in the press).
35. Wiesmann, K. E. H. *et al. Chem. Biol.* **2**, 583–589 (1995).

ACKNOWLEDGEMENTS. This work was supported by the NIH, a National Science Foundation Young Investigator Award (C.K.) and a David and Lucile Packard fellowship for Science and Engineering (C.K.).

Global interdecadal and century-scale climate oscillations during the past five centuries

Michael E. Mann*, Jeffrey Park* & R. S. Bradley†

* Department of Geology and Geophysics, Yale University, PO Box 208109, New Haven, Connecticut 06520-8109, USA

† Department of Geosciences, University of Massachusetts, Amherst, Massachusetts 01003, USA

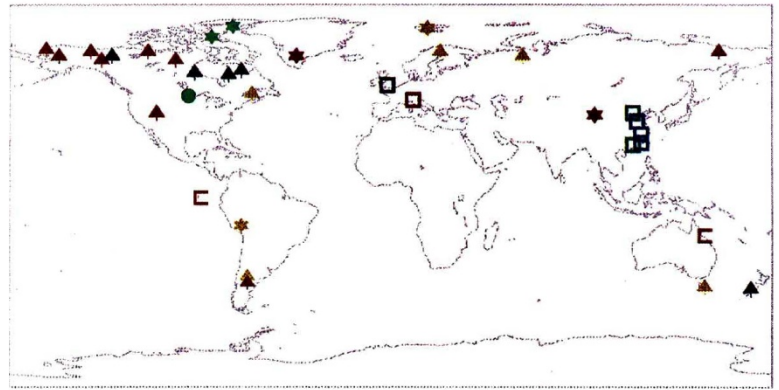
THE recognition of natural modes of climate variability is essential for a better understanding of the factors that govern climate change. Recent models suggest that interdecadal (roughly 15–35-year period)^{1–4} and century-scale (roughly 50–150-year period)^{5–7} climate variability may be intrinsic to the natural climate system. While there is some evidence for the existence of interdecadal^{8,9} and century-scale^{9,10} oscillations in instrumental temperature records, confident detection from these short (100–400-year) records is difficult^{11,12}. Oscillations on the same timescales^{5,13–17} have also been detected in isolated climate-proxy or historical records over longer durations, but the large-scale spatial structure of the variability has not been investigated systematically. Here we report the multivariate analysis of a globally distributed set of temperature proxy records of several centuries duration. The results of our spatio-temporal analysis strengthen evidence for persistent natural interdecadal and century-scale climate oscillations, and reveal both the spatial patterns and temporal histories of these signals.

Evidence for truly global climate signals must demonstrate consistent variations in data from widely separated localities, using records that are long enough to resolve the timescales of interest. To isolate possible climate signals, we have compiled a small (35), but globally distributed, set of high-quality temperature proxy reconstructions (Fig. 1) for the past five centuries. These data include tropical¹⁸ and extratropical¹⁹ ice cores, tropical corals (ref. 14 and J. Lough, personal communication) dendroclimate reconstructions (refs 19–21 and C. Earle, personal communication) and a handful of very long historical records¹⁹. Some seasonal inhomogeneity may be present in these data series because the extratropical records, unlike the tropical records, chiefly reflect summer season variability¹⁹. However, recent analyses²² suggest that large-scale, low-frequency surface temperature variability is largely independent of the seasonality of sampling. Thus we expect that such inhomogeneity will have little impact on signal detection. We employed a frequency-domain singular value decomposition (SVD) method that is designed to isolate and reconstruct quasiperiodic or unstable oscillations that are spatially coherent but which may exhibit phase-lags from site to site^{9,23}.

The sparseness of the data set argues for a cautious interpretation, but the analysis suggests greater potential of our spatio-temporal approach applied to expanded networks of climate-proxy data. We balanced spatial coverage, duration and time resolution (annual versus decadal) by grouping the proxy data into four subsets that were analysed independently: A, 27 shorter records (AD 1730–1969) with annual resolution; B, 21 medium-duration (AD 1615–1969) records with annual resolution; C, 35 shorter (AD 1730–1960) records with decadal resolution; and D, 12 longer (AD 1400–1960) records with decadal resolution.

We compared the proxy network against instrumental data in sampling large-scale climate variability. We performed parallel

FIG. 1 Distribution of proxy temperature reconstructions used in the present study. Squares, historical records; circles, lake varves; stars, ice-core/ice-melt measurements, stemmed triangles, dendroclimate reconstructions; "C" symbols, coral reconstructions. In contrast with other reconstructions, the dendroclimate reconstruction corresponding to the indicated southwestern US 'site' was actually based on the spatial averaging of data over a larger region¹⁹. Records indicated by yellow are available from AD 1400 to 1969 and have annual resolution; records indicated by green are available from AD 1400–1960 and have decadal sampling, red symbols correspond to records available from 1615–1969 with annual resolution, blue symbols records from 1620 to 1960 with decadal sampling, black symbols records from 1730–1969 with annual resolution. Thus, data group A makes use of the 27 yellow, red and black records, data group B the 21 yellow and red records, data group C all 35 records, and data group D the 12 yellow and green records.



analyses of data during the past century based on (1) the global distribution of instrumental temperature data from 1890 to 1989 used by Mann and Park⁹, (2) proxy data set A using the abbreviated interval 1890–1969, and (3) a sparse sub-sampling of the instrumental data during the interval 1890–1969 chosen to mimic the spatial distribution and seasonal sampling of the proxy data. A perfect spatial match between data sets (2) and (3) is not possible, largely due to a paucity of high-latitude instrumental data. The 'SVD spectra' in Fig. 2 show the fraction of data variance in a narrow frequency range that can be explained by a single correlated signal. All three data sets exhibit correlated interdecadal (15–20-year period) variability that we estimate as significant at the 95% confidence level. A roughly decadal (10–12-year) peak corresponding to variability in the high-latitude North Atlantic Ocean and North America during the past century^{9,23} is less consistently observed. Within the secular regime (corresponding to periods greater than the 40 (2) and (3) or 50 (1) years), two distinct modes of variability are significant in each data set, corresponding to a secular warming trend and a weaker variation that resembles one cycle of a century-scale oscillation. The associated spatial patterns of variation (not shown) of these signals in cases (2) and (3) are broadly consistent with their counterparts in (1) shown by Mann and Park⁹. The proxy data network thus seems capable of capturing the large-scale climate processes evident in recent instrumental-based analyses, at least on certain timescales.

The SVD spectra corresponding to the full-length series for data groups A–D (Fig. 3) yield statistically significant peaks on roughly interdecadal (15–35-year) and century (50–150-year) timescales. We isolate a quarter-millennial (~240 year) oscillation in data group D where longer-period variability can be resolved from a secular trend. This identification is tentative, however, as less than three 'cycles' are present, and the signal cannot be independently confirmed from the other data groups. Only groups A and B can properly resolve the interdecadal signals, as the Nyquist frequency for 10-year sampling corresponds to a 20-year period. Higher-frequency signals related to the El Niño/Southern Oscillation (ENSO) that are observed in the A and B analyses²⁴ will be discussed elsewhere. Comparing the spatial patterns of the interdecadal and century-scale signals reveals distinctions that are consistent among the data groups. Peaks of correlated variance fall roughly into interdecadal and century-scale bands. The variation of the location and magnitude of the peaks within these bands suggests quasiperiodic signals with amplitudes and frequencies that drift over time.

The time-evolving amplitude and frequency of quasiperiodic signals can be examined with an 'evolutionary' analysis (Fig. 4), in which the SVD analysis is applied in a moving window through the data series. The short duration, combined with decadal resolution, precludes a meaningful evolutionary analysis for data group

C. Evolutionary analyses of the other data groups demonstrate that coherent interdecadal oscillations, centred near 20–25-year periodicity, were weakly evident before 1800. The oscillations subsequently strengthen in significance and drift to roughly 16–18-year period in the final window (1869–1969), which agrees with the dominant timescale of oscillations observed in instrumental surface-temperature data⁹ during the past century. Time windows that resolve century-scale variations (200-year width) can be employed for data group D. Before 1650, a coherent signal with roughly 50-year period appears intermittently. After 1650 this oscillation strengthens in its significance and drifts to a 60–70-year periodicity. In the nineteenth century, these 'century-scale' oscillations seem to drift to slightly longer period, becoming indistinguishable from secular variability in a 200-year moving window. The improved frequency resolution of data group D allows for a clearer separation of the interdecadal and century-scale variability than is possible with groups A and B.

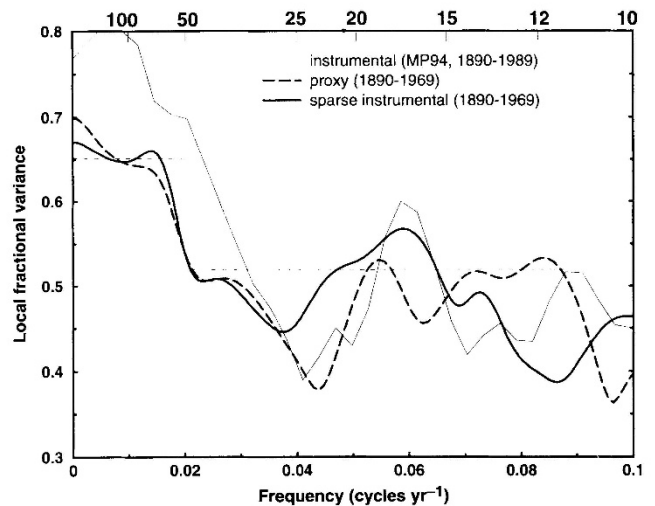


FIG. 2 SVD spectra (local fractional variance explained by principal mode in the SVD within a narrow band about a specified carrier frequency as a function of frequency—see Fig. 3) for (1) instrumental data of Mann and Park⁹ (thin solid line), (2) proxy data set A (dashed line), (3) sparse distribution of instrumental data as described in the text (thick solid line). The local fractional variance scale corresponds to (1), with the scales adjusted for (2) (−0.03), (3) (−0.07) to align the position of the 95% confidence level owing to varying effective spatial degrees of freedom in the different analyses. Confidence limits are higher within the secular band (corresponding to variability longer than half the record lengths) owing to decreased spectral degrees of freedom near zero frequency.

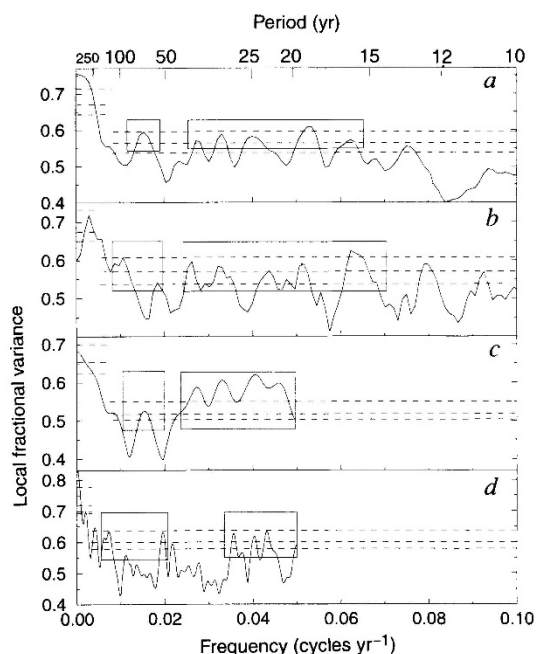


FIG. 3 SVD spectra for each of the data group. A–D. (see Fig. 1 legend) The spectra are plotted as in Fig. 2 but with the 90%, 95%, and 99% confidence limits (dashed lines) each shown. Boxes group spectral peaks into ~15–35-year interdecadal, and ~50–150-year century-scale, bands.

METHODS. We calculate the tapered Fourier transform of a set of M time series of uniform length of N years, using multitaper spectral analysis to provide a small number (K) of independent spectral estimates for each time series $x_{(m)}$ in a narrow frequency band centred at frequency f ,

$$y_k^{(m)}(f) = \sum_{n=1}^N w_n^{(k)} x_n^{(m)} e^{i2\pi f n \Delta t}$$

where $\Delta t=1$ month is the sampling interval and $\{w_n^{(k)}\}_{n=1}^N$ is the k th member in an orthogonal sequence of leakage-resistant data tapers. We construct the $M \times K$ matrix

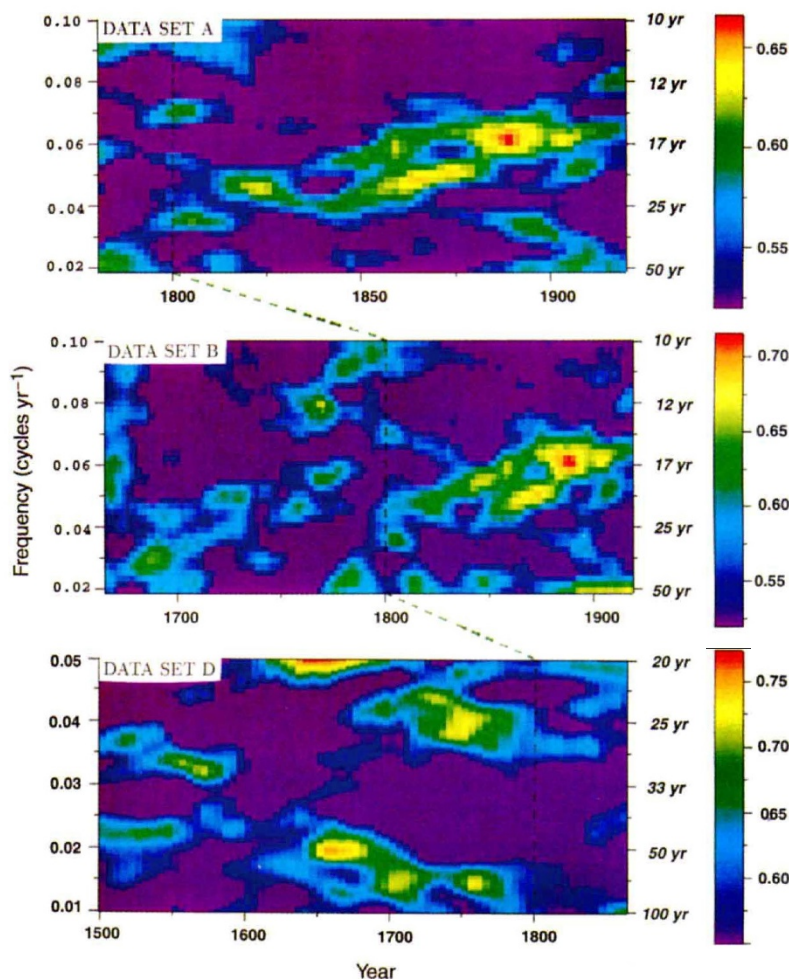
$$\mathbf{A}(f) = [\omega_m y_k^{(m)}(f)]$$

where $m=1, \dots, M, k=1, \dots, K$, each row calculated from a different grid-point time series (normalized by its standard deviation). We use $K=3$ as a trade-off between spectral resolution and degrees of freedom. The relative weights for different series (ω_m) are chosen so that a large number of nearby sites do not combine to have disproportional weight in the analysis. We perform the complex singular value decomposition,

$$\mathbf{A}(f) = \sum_{k=1}^K S_k(f) \mathbf{u}_k(f) \otimes \mathbf{v}_k^*(f)$$

into K orthonormal left (\mathbf{u}_k^*) and right (\mathbf{v}_k) eigenvectors, which can be used to recover spatial and temporal patterns, respectively. The singular value $S_k(f)$ scales the amplitude of the k th mode. The spectrum of 'local' fractional variance explained by the principal mode is described by $S_1^2(f)/\sum_{k=1}^K S_k^2(f)$, with narrow peaks in the spectrum indicating potential quasiperiodic signals. Confidence limits for peak significance are obtained by resampling methods⁹.

FIG. 4 Evolutive SVD spectra. A common year (AD 1800) is indicated by a thick dashed line to allow visual alignment of the time axes for the three plots shown. For each case, the local fractional variance spectrum is indicated by a colour scale shown to the right of the plot. The colour convention is chosen so that any features clearly visible above the background are significant well above the 95% level. Window timelengths τ_w are chosen to be long enough to allow high-frequency resolution, while being short enough to provide insight into the evolving character of signals. The centre of the moving windows defines its time coordinate, so information for the first and last $\tau_w/2$ years are lost. Periods longer than $\tau_w/2$ cannot be distinguished from secular variability in the evolutive analyses, and are not shown. Top panel, Evolutive SVD spectrum for data group A using a 100-year moving window evaluated in 2-year steps. Century-scale variability cannot adequately be distinguished from significant secular (>50-year timescale) variability for this data group. Significance levels for the local fractional variance spectrum are given by 90% (0.55), 95% (0.565) and 99% (0.60). Middle panel, Evolutive SVD spectrum for data group B using a 100-year moving window evaluated in 2-year steps. The significance levels are the same as for data group A. Bottom panel, Evolutive SVD spectrum for data group D using a 200-year moving window evaluated in 5-year steps. For this data subset, century-scale oscillations are largely resolved (although variability on timescales longer than 100 years is indistinguishable from the secular band). Significance levels are given by 90% (0.58), 95% (0.60) and 99% (0.64). Note the different frequency/period scale in this case.



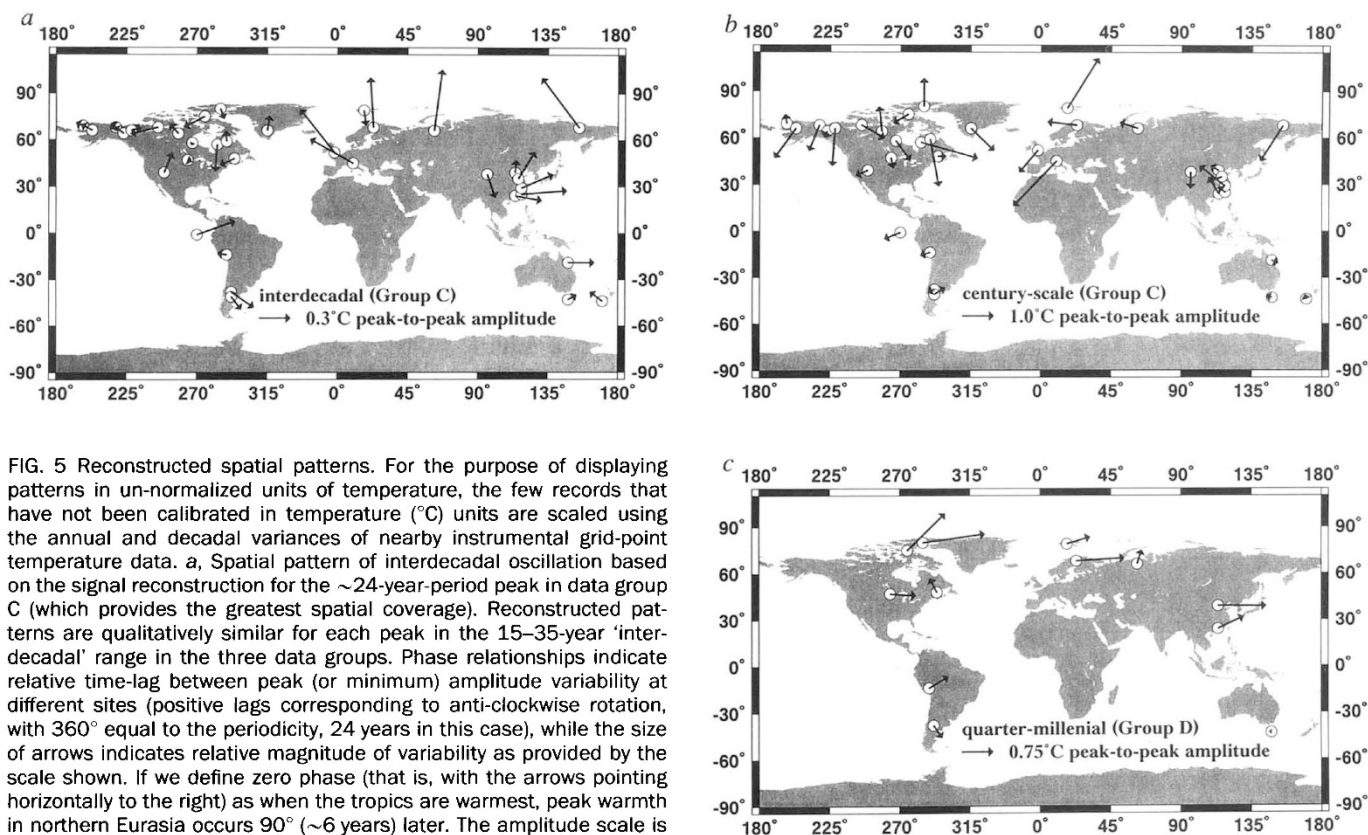


FIG. 5 Reconstructed spatial patterns. For the purpose of displaying patterns in un-normalized units of temperature, the few records that have not been calibrated in temperature ($^{\circ}\text{C}$) units are scaled using the annual and decadal variances of nearby instrumental grid-point temperature data. *a*, Spatial pattern of interdecadal oscillation based on the signal reconstruction for the ~ 24 -year-period peak in data group C (which provides the greatest spatial coverage). Reconstructed patterns are qualitatively similar for each peak in the 15–35-year ‘interdecadal’ range in the three data groups. Phase relationships indicate relative time-lag between peak (or minimum) amplitude variability at different sites (positive lags corresponding to anti-clockwise rotation, with 360° equal to the periodicity, 24 years in this case), while the size of arrows indicates relative magnitude of variability as provided by the scale shown. If we define zero phase (that is, with the arrows pointing horizontally to the right) as when the tropics are warmest, peak warmth in northern Eurasia occurs 90° (~ 6 years) later. The amplitude scale is set so that the largest arrow corresponds to the regional maximum amplitude of the oscillation of $\sim 0.6^{\circ}\text{C}$ peak-to-peak. *b*, Spatial pattern for century-scale signal oscillation reconstructed for the 65-year-period variance peak of data group C. Plot conventions are analogous to those in *a*, with 360° phase difference associated with a 65-year period. The pattern maximum is $\sim 2^{\circ}\text{C}$ peak-to-peak oscillation (for example, central

Figure 5 shows reconstructions of the spatial patterns of variation for the interdecadal (panel *a*), century-scale (*b*) and quarter-millennial (*c*) signals. In the spatial reconstructions, sources of systematic bias in the individual temperature reconstructions may lead to unreliable phase and amplitude at specific sites. Calibration of proxy data at longer periods, and various corrections that are made to proxy records (for example, subtraction of individual long-term growth trends for dendroclimate records) are potential sources of such bias. Thus, it is the regional trends evident in these patterns that are most meaningful.

The interdecadal signal (Fig. 5*a*) exhibits variability in the tropics and subtropics that is largely in-phase. Mid-latitude variations are of similar magnitude, but phase relationships are more variable, consistent with the signature of extratropical teleconnection patterns. Such patterns can be resolved by our data network only in part. Nevertheless, the alternating pattern of phase from Greenland, to eastern and then western mid-latitude North America (with a nodal point in central North America) is consistent with the alternating warm and cold advection of the three-lobed ‘Pacific North American’ pressure anomaly pattern. In-phase tropical/extratropical temperature variability coupled with such an extratropical pattern has been noted as a signature of the global-scale ENSO phenomenon in instrumental records^{9,25}. Studies of both instrumental climate data^{9,23,26} and isolated long-term proxy records²⁷ suggest that interdecadal climate variability is closely associated with the Pacific North American pattern. A connection has also been found with low-frequency changes in ENSO²⁶. Although the dynamics of such a linkage are still unclear, our study indicates a possible long-term connection between interdecadal climate oscillations and

Europe). *c*, Spatial pattern for the quarter-millennial oscillation. Variations are largely in phase, spread out (with a few exceptions) over ~ 90 – 120° in phase (that is, 60–80 years). The pattern maximum is a $\sim 1.5^{\circ}\text{C}$ peak-to-peak oscillation.

low-frequency changes in ENSO. Recent model simulations indicate that the origin of this variability may lie in extratropical ocean–atmosphere interaction³.

The pattern of the century-scale mode (Fig. 5*b*) exhibits high-amplitude variability largely confined to the North Atlantic and Arctic, out-of-phase with weaker variability in the Pacific basin. These features resemble the pattern of a single ‘oscillation’ detected in a century of gridded surface temperature data^{9,10}. Apart from the Svalbard site in the boreal Atlantic, there is a tendency towards opposing, though not opposite, phase anomalies (that is, $\sim 45^{\circ}$ – 135° phase difference) between the eastern and western margins of the North Atlantic. Such a phase pattern suggests a combination of in-phase and out-of-phase components in the two regions. An out-of-phase component could arise from differential temperature advection on either side of an alternating centre of low and high pressure over the North Atlantic. Changes in northward oceanic heat transport would generate an in-phase component of basinwide warming and cooling. The combination of these effects is consistent with coupled ocean–atmosphere model simulations⁷, in which century-scale (40–60-year) oscillations in sea-level pressure over the North Atlantic coincide with oscillations in the thermohaline circulation.

The quarter-millennial oscillation has a spatial pattern that is largely in-phase globally, although the phase-lags in the reconstruction correspond to time-lags as large as 100 years between warm or cold periods at different sites. The time reconstruction (not shown) suggests that this oscillation describes a global-scale transition from warmer conditions before 1500 to the colder conditions of the sixteenth to eighteenth centuries^{19,28}.

We find some empirical evidence for persistent, if variable, low-frequency global-scale climate oscillations on interdecadal

and century timescales. The spatial reconstructions of these signals provide material for hypotheses about the possible underlying processes, for example, a connection between interdecadal climate variations and low-frequency ENSO variability, and a connection between persistent century-scale oscillations and low-frequency variability in the thermohaline circulation. Although such hypotheses are speculative given the limited spatial distribution of the present dataset, they can be tested more rigorously with similar analyses of the expanding network of high-quality climate-proxy reconstructions. □

Received 23 February; accepted 25 September 1995.

1. Barnett, T. P., Del Genio, A. D. & Ruedy, R. A. *J. geophys. Res.* **97**, 7341–7354 (1992).
2. Von Storch, J. S. *Tellus* **46**, 419–432 (1994).
3. Latif, M. & Barnett, T. P. *Science* **266**, 634–637 (1994).
4. Chen, F. & Ghil, M. *J. phys. Oceanogr.* (in the press).
5. Stocker, T. F. & Mysak, L. *Clim. Change* **20**, 227–250 (1992).
6. Mysak, L. A., Stocker, T. F. & Huang, F. *Clim. Dyn.* **8**, 103–116 (1993).
7. Delworth, T., Manabe, S. & Stouffer, R. J. *J. Clim.* **6**, 1993–2011 (1993).
8. Ghil, M. & Vautard, R. *Nature* **350**, 324–327 (1991).
9. Mann, M. E. & Park, J. *J. geophys. Res.* **99**, 25819–25833 (1994).
10. Schlesinger, M. E. & Ramanakutty, N. *Nature* **367**, 723–726 (1994).
11. Elsner, J. B. & Tsonis, A. A. *Nature* **372**, 507–508 (1994).
12. Schlesinger, M. E. & Ramanakutty, N. *Nature* **372**, 508–509 (1994).
13. Diaz, H. & Pulwarty, R. S. *Clim. Change* **26**, 317–342 (1994).
14. Dunbar, R. B., Wellington, G. M., Colgan, M. W. & Glynn, P. W. *Paleoceanography* **9**, 291–315 (1994).
15. Linsley, B. K., Dunbar, R. B., Wellington, G. M. & Mucciarone, D. A. *J. geophys. Res.* **99**, 9977–9994 (1994).
16. Plaut, G., Ghil, M. & Vautard, R. *Science* **268**, 710–713 (1995).
17. Thomson, D. J. *Phil. Trans. R. Soc. Lond. A* **330**, 601–616 (1990).
18. Thompson, L. in *Climate Since A.D. 1500* (eds Bradley, R. S. & Jones, P. D.) 517–548 (Routledge & Kegan Paul, Boston, 1992).
19. Bradley, R. S. & Jones, P. D. *Holocene* **3**, 367–376 (1993).
20. Jones, J. D. & Briffa, K. R. *Holocene* **1**, 165–179 (1992).
21. Jacoby, G. C. & D'arrigo, R. *Clim. Change* **14**, 39–59 (1989).
22. Briffa, K. R. & Jones, P. D. *Holocene* **3**, 82–92 (1993).
23. Mann, M. E., Lall, U. & Saltzman, B. *Geophys. Res. Lett.* **22**, 937–940 (1995).
24. Bradley, R. S., Mann, M. E. & Park, J. *Eos (suppl.)* **75**, 383 (1994).
25. Halpert, M. S. & Ropelewski, C. F. *J. Clim.* **5**, 577–593 (1992).
26. Trenberth, K. *Bull. Am. met. Soc.* **71**, 988–993 (1990).
27. Slowey, N. C. & Crowley, T. J. *Geophys. Res. Lett.* **22**, 2345–2348 (1995).
28. Hughes, M. & Diaz, H. F. *Clim. Change* **26**, 109–129 (1995).

ACKNOWLEDGEMENTS. We thank G. Jacoby and L. Thompson for providing several data series used in this study, and B. Saltzman for comments on the manuscript. This work was supported by the US NSF (M.E.M., J.P. and R.B.) and the US Department of Energy (R.B.).

The 'Daly gap' as a magmatic catastrophe

C. C. Bonnefoi*†, A. Provost* & F. Albarède†

* Université de Clermont-Ferrand, Département des Sciences de la Terre, 63038 Clermont-Ferrand Cedex, France

† Ecole Normale Supérieure de Lyon, 69364 Lyon Cedex 7, France

IGNEOUS rocks very commonly show a strongly bimodal distribution of compositions, one mode corresponding to basalt and the other to felsic magmas^{1–3}. As fractional crystallization of basaltic parents produces a continuum of compositions, the paucity of rocks of intermediate composition—commonly called the Daly gap—has puzzled petrologists since the time of Daly. Gravitational or viscous trapping^{4,5}, large crystal loads restraining convection^{6,7}, and re-melting of deep volcanic layers² are among the processes that have been offered as physically meaningful explanations of magmatic gaps. Here we propose an alternative interpretation, transposed from chemical reactor control theory⁸: at large undercooling, thermal feedback in a continuously fed and differentiating magma reservoir promotes the existence of competing thermochemical steady states. Small variations in magma residence time and cooling rate induce a large thermal and chemical swing (magmatic bifurcation or catastrophe), which interrupts the liquid line of descent, leading to bimodal erupted products.

We consider a differentiating magma reservoir continuously erupting, crystallizing, and replenished (Fig. 1). The temperature

and composition of the liquid are assumed to be homogeneous within the reservoir, which implies vigorous convection at rather high Rayleigh numbers such as in vertical dykes. Input magmas are crystal-free. The output at first consists of erupted lavas, which initially are assumed to be aphyric (crystal-free), although this assumption is in no way critical. In addition, a mass of cumulate mush fills up the bottom of the reservoir while continuing replenishment by fresh magma is accommodated by the wall rocks being moved apart. The reservoir is defined as the liquid part of the magmatic system. Crystallization changes liquid composition and releases latent heat while the reservoir loses heat by conduction or hydrothermal convection to its surroundings. In our analysis, the following symbols are used: t for time, T for temperature, M for the mass of a phase, Q for magma input/output rate, C_p for heat capacity, L for latent heat, and Φ for the rate of heat loss. Liquid and solid are referred to by the subscripts _{liq} and _{sol}, respectively, input and output by the subscripts _{in} and _{out}.

Mass balance between input, output, and crystal accumulation on the floor and walls of the reservoir requires

$$\frac{dM_{\text{liq}}}{dt} = Q_{\text{in}} - Q_{\text{out}} - \dot{M}_{\text{sol}} \quad (1)$$

where the overdot refers to the rate of change. Similarly, the heat-conservation condition is given by

$$\frac{d[M_{\text{liq}}(C_p T_{\text{liq}} + L)]}{dt} = Q_{\text{in}}(C_p T_{\text{in}} + L) - Q_{\text{out}}(C_p T_{\text{liq}} + L) - \dot{M}_{\text{sol}} C_p T_{\text{sol}} - \Phi \quad (2)$$

Temperature is assumed to be identical in the liquid and in the last increment of cumulate. For constant T_{in} , these equations are reformulated accordingly with respect to a single state-variable, the dimensionless cooling $v = 1 - T_{\text{liq}}/T_{\text{in}}$ as

$$\frac{dv}{dt} = -\frac{v}{\tau} + \frac{\eta + 1}{\theta} - \eta \dot{f} \quad (3)$$

where $\dot{f} = \dot{M}_{\text{sol}}/M_{\text{liq}}$ is the fractional rate of solidification. The system has three control parameters: $\tau = M_{\text{liq}}/Q_{\text{in}}$ the magma residence time in the reservoir, $\theta = M_{\text{liq}}(L + C_p T_{\text{in}})/\Phi$ the Newtonian cooling time, and $\eta = L/(C_p T_{\text{in}})$ the reduced latent heat.

If all control parameters stay constant, the system approaches a steady state with a relaxation time on the order of τ . It is not thus implied that natural systems are time-independent, but this assumption provides a convenient illustration of how a magmatic catastrophe may develop over periods longer than τ . To understand the source of instabilities, we investigate how the thermal regime of the reservoir depends on the rate of replenishment. Equation (3) at thermal steady-state is rewritten as a balance between latent heat release and advection-conduction effects

$$\eta \dot{f} = \frac{\eta + 1}{\theta} - \frac{v}{\tau} \quad (4)$$

Both linear crystal growth rate G and nucleation rate I cancel at the liquidus and below the glass transition. Upon cooling, both G and I therefore go through a maximum at an intermediate temperature⁹. Deferring justification to later in the Letter, we assume that the rate of solidification \dot{f} is also a bell-shaped function of temperature. The righthand side of equation (4) is the equation of a straight line Δ with slope $-1/\tau$, vertical intercept $(\eta + 1)/\theta = \Phi/(M_{\text{liq}} C_p T_{\text{in}})$, and horizontal intercept $(\eta + 1)\tau/\theta$ (Fig. 2a). Any intersection between the curve $\eta \dot{f}(v)$ and Δ is a solution of equation (4). For very high cooling rates, ($\theta = \theta_1$ in Fig. 2a), there is only one such intersection regardless of the magma residence time τ . For slower cooling ($\theta = \theta_2$), increasing the magma residence time shifts the system from one to three intersections, then from three to one. The system bifurcates when the straight line Δ becomes tangent to the curve $\eta \dot{f}(v)$. In the case of three intersections A, B and C, the intermediate steady